

Backward propagating acoustic waves in single gold nanobeams

Cyril Jean, Laurent Belliard, Loïc Becerra, and Bernard Perrin

Citation: [Applied Physics Letters](#) **107**, 193103 (2015); doi: 10.1063/1.4935351

View online: <http://dx.doi.org/10.1063/1.4935351>

View Table of Contents: <http://scitation.aip.org/content/aip/journal/apl/107/19?ver=pdfcov>

Published by the [AIP Publishing](#)

Articles you may be interested in

[Efficient excitation of guided acoustic waves in semiconductor nanorods through external metallic acoustic transducer](#)

Appl. Phys. Lett. **105**, 243101 (2014); 10.1063/1.4904414

[Plane wave propagation in generalized multiply connected acoustic filters](#)

J. Acoust. Soc. Am. **118**, 2860 (2005); 10.1121/1.2049127

[A mixed finite element method for acoustic wave propagation in moving fluids based on an Eulerian–Lagrangian description](#)

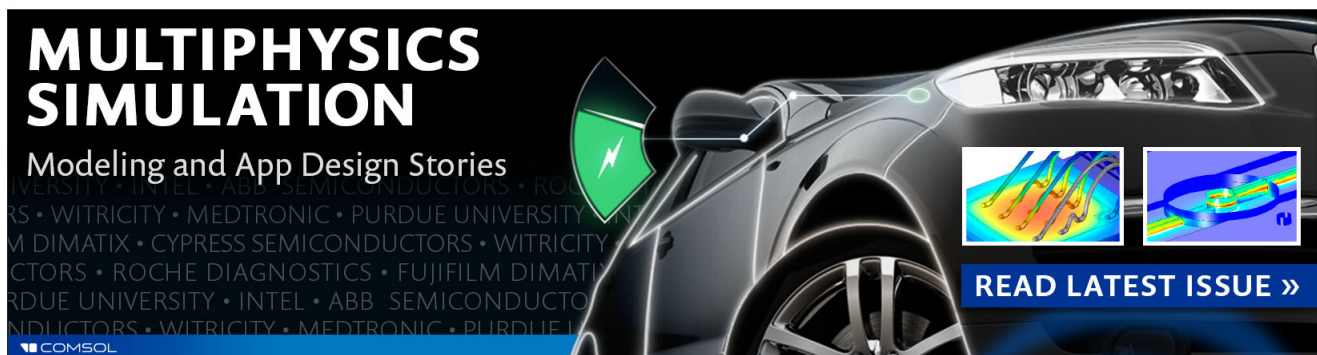
J. Acoust. Soc. Am. **113**, 705 (2003); 10.1121/1.1534837

[Wave propagation in range-dependent poro-acoustic waveguides](#)

J. Acoust. Soc. Am. **104**, 783 (1998); 10.1121/1.423239

[Acoustic propagation through an internal wave field in a shallow water waveguide](#)

J. Acoust. Soc. Am. **101**, 789 (1997); 10.1121/1.418039

The advertisement features a dark background with a car's front end on the right. On the left, the text 'MULTIPHYSICS SIMULATION' is written in large, bold, white letters. Below it, 'Modeling and App Design Stories' is written in a smaller white font. A green lightning bolt icon is positioned between the text and the car. On the right side of the car, there are two small inset images showing simulation results: one with a color gradient and another with a blue and yellow pattern. At the bottom right, a blue button with white text says 'READ LATEST ISSUE >>'. The COMSOL logo is in the bottom left corner.

**MULTIPHYSICS
SIMULATION**

Modeling and App Design Stories

READ LATEST ISSUE >>

COMSOL

Backward propagating acoustic waves in single gold nanobeams

Cyril Jean, Laurent Belliard,^{a)} Loïc Becerra, and Bernard Perrin
 Sorbonne Universités, UPMC Univ Paris 06, CNRS-UMR 7588, Institut des NanoSciences de Paris,
 F-75005 Paris, France

(Received 30 September 2015; accepted 25 October 2015; published online 9 November 2015)

Femtosecond pump-probe spectroscopy has been carried out on suspended gold nanostructures with a rectangular cross section lithographed on a silicon substrate. With a thickness fixed to 110 nm and a width ranging from 200 nm to 800 nm, size dependent measurements are used to distinguish which confined acoustic modes are detected. Furthermore, in order to avoid any ambiguity due to the measurement uncertainties on both the frequency and size, pump and probe beams are also spatially shifted to detect guided acoustic phonons. This leads us to the observation of backward propagating acoustic phonons in the gigahertz range (~ 3 GHz) in such nanostructures. While backward wave propagation in elastic waveguides has been predicted and already observed at the macroscale, very few studies have been done at the nanoscale. Here, we show that these backward waves can be used as the unique signature of the width dilatational acoustic mode.
 © 2015 AIP Publishing LLC. [<http://dx.doi.org/10.1063/1.4935351>]

Probing the elasticity at the nanoscale is a challenge that led a wide community to study confined acoustic modes of nano-objects in the 10 GHz–1 THz range using time-resolved pump-probe experiments.¹ In such an approach, acoustic modes are excited by the absorption of a femtosecond laser pulse and detected in transmission^{2,3} or reflectivity geometry in near^{4,5} or far^{6,7} field by the induced change in the material optical properties. As ensemble studies result in inhomogeneous broadening of the acoustic features,^{8,9} single particle spectroscopy has been considered to circumvent this drawback and to clarify the acoustic response.^{3,10,11} However, the strong damping at these extremely high frequencies has led several groups to isolate the nanoresonators from their substrate to avoid energy leaking through the nano-object-substrate contact.^{12–14} These breakthroughs have made possible the observation of an other source of acoustic energy leaks. Indeed, it has been proven that acoustic phonons are also guided along the nano-objects.^{15,16} Other major developments illustrate the possibility to use nano-objects as nanoscale acoustic transducers for hypersonic wave imaging.¹⁷ Non destructive imaging with nanometric resolution in both depth and lateral direction is now one step ahead.

Furthermore, there is a recent and growing interest in both the electromagnetic and acoustic wave communities for materials and waveguides that exhibit backward propagating waves.¹⁸ In backward waves, the phase velocity describing the propagation of individual wave fronts in a wave packet and the energy flux of the wave, characterized by the Poynting vector, are anti-parallel. This anti-parallel propagation constitutes the definition of a negative index material and opens the way to a large variety of intriguing physical phenomena.¹⁹ There now exist multiple experimental evidences of this effect, and applications of negative index materials for electromagnetic waves have already been conceived.²⁰ The possibility of such backward wave motion in elastic waveguides has been revealed by the early work of

Lamb.²¹ Many different elastic waveguides such as cylinders²² or surface acoustic waves²³ can also exhibit backward wave motion. Recently, negative refraction and focusing of elastic Lamb waves have been investigated but are still confined to the low-MHz range.^{24,25} In this letter, we provide evidence of backward wave propagation in one-dimensional elastic waveguide in the gigahertz range. We use time-resolved pump-probe spectroscopy with spatially shifted pump and probe beams to excite and detect the backward wave motion. As a first application, unambiguous mode identification using backward wave propagation is investigated.

In order to study guided modes in one dimensional elastic waveguides, gold nanostructures with a rectangular cross section are conceived (Fig. 1). Their thickness, h , is fixed to $h = 110$ nm and their width, W , ranges from 200 to 800 nm.

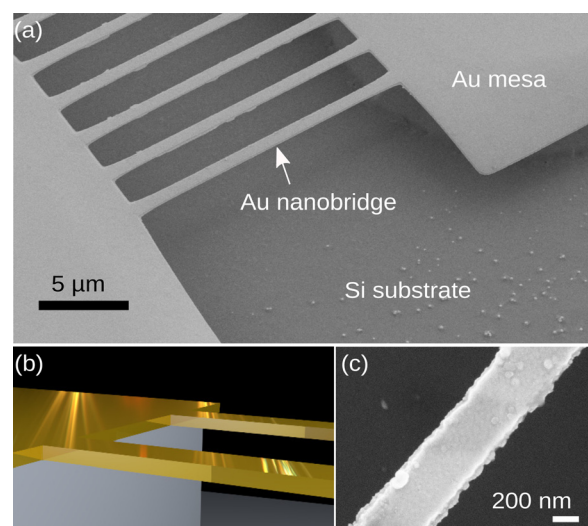


FIG. 1. (a) Scanning electron microscope image (top view) of several gold nanobeams suspended a few micrometers above the silicon substrate. (b) Artist view of nanobeams with a rectangular cross section suspended above the silicon substrate. (c) Scanning electron microscope image (top view) of a 400 nm wide gold nanobeam. The edge roughness is lower than 20 nm.

^{a)}Laurent.Belliard@upmc.fr

As shown in Fig. 1(a), the gold stripes are connected to large mesas at both ends. To reduce the influence of the silicon substrate on the elastic confinement, the gold nanostructures are suspended several micrometers above the substrate as illustrated in Fig. 1(b). This geometry results in what we call “gold nanobeams.” All boundaries are thus mechanically free. As their length is greater than $15\ \mu\text{m}$, they are considered as infinitely long and the fixed boundary conditions at the extremities can be neglected. The samples are fabricated by electronic lithography coupled with anisotropic wet etching on silicon substrates. To prepare these structures, single face polished Si(001) substrates are used. First, an electronic resist (PMMA-950 K-A6) is spin coated on the Si wafer surface. The exposition is made at 20 kV using a Zeiss Supra 40 scanning electron microscope equipped with a Raith Elphy Quantum module. After being developed, rinsed with water and blown dry, the sample is coated with 10 nm of chromium to improve the adhesion, followed by a 110 nm thick gold layer. Then, a lift-off process in acetone with careful ultrasonic agitation is performed to delimit the future gold nanobeams. Finally, the sample is dipped in a hot 40% KOH solution to partially etch the Si substrate and free the desired gold nanobeams. This quick anisotropic Si etching process leads to the formation of suspended gold nanobeams between two big gold pads. The key point of this process is that the main axis of the beams has been rotated 45° with respect to the $\langle 110 \rangle$ direction of Si substrates to allow this underetching.

Our experimental setup working in reflection geometry was described in detail elsewhere.⁷ Ultrafast pump-probe spectroscopy experiments are performed using a mode-locked Ti:sapphire (MAI-TAI Spectra) laser source operating at 800 nm with a pulse duration below 100 fs at the laser output and a repetition rate of 78.8 MHz. Synchronous detection on the sample reflectivity is performed by modulating the pump beam at 1.8 MHz. Both pump and probe beams are focused by means of a microscope objective with a $NA = 0.9$ and are normally incident on the sample. The laser spots can be focused around $1\ \mu\text{m}$ diameter at $1/e^2$. A telescope is fixed on a XY piezoelectric stage such that the probe beam is laterally positioned with respect to the fixed pump beam. A two-color experiment is performed by doubling the pump frequency ($\lambda = 400\ \text{nm}$) with a nonlinear crystal (BBO) to avoid scattered light coming from the pump beam. A dichroic filter located in front of the diode system suppresses the light of the pump beam, its power is reduced around $500\ \mu\text{W}$, and the power of the probe beam does not exceed $15\ \mu\text{W}$.

Such experimental conditions place us in the thermo-elastic regime and the acoustic signal and optical reflectivity remain stable during all the average processing. The reflectivity from the sample is measured by an avalanche photodiode and analyzed with a lock-in amplifier. A maximum pump-probe time delay equal to 12 ns is achieved using a mobile reflector system mounted on a translation stage.

First, let us consider the case where the pump and probe beams are spatially superimposed. Fig. 2 shows the time domain reflectivity change measurements $\Delta R/R$ obtained on a $400\ \text{nm} \pm 20\ \text{nm}$ wide (determined by SEM measurement) and 110 nm thick gold nanobeam in a usual reflectometry

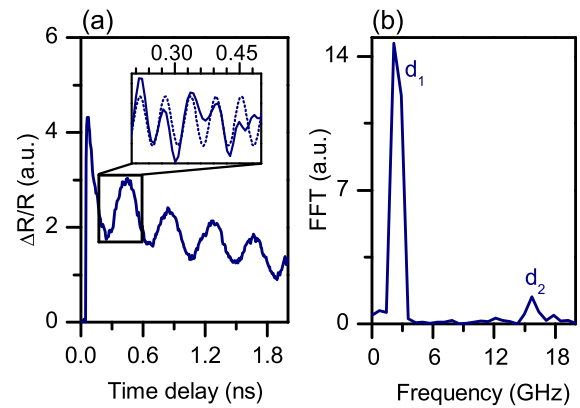


FIG. 2. (a) Typical time-resolved modulation of the reflected probe beam $\Delta R/R$ of a $400\ \text{nm} \pm 20\ \text{nm}$ wide and 110 nm thick gold nanobeam that exhibits a low frequency oscillation at 2.8 GHz superimposed to a higher modulation around 16 GHz (the inset is a zoom where the lower modulation is removed; dotted line is a 16 GHz sinus). (b) Fourier power spectra of the time transient signal (a) showing both 2.8 GHz and 16 GHz acoustic signatures. d_1 and d_2 refer to the first dilatational modes.

set-up. After a sharp and sudden rise, a slowly decreasing non-oscillatory background in $\Delta R/R$ is observed. This is the signature of the rapid heating of the electron gas induced by the pump pulse absorption, followed by the slow cooling down process. This thermal stress launches the acoustic vibrations of the nanobeam.²⁶ The time-resolved signature also shows a superposition of high (inset Fig. 2(a)) and low frequency oscillations. By performing a numerical fast Fourier transform (Fig. 2(b)) or by fitting the time oscillation with a damped sinus function, one can extract a $2.8\ \text{GHz} \pm 0.5\ \text{GHz}$ and a $16\ \text{GHz} \pm 0.5\ \text{GHz}$ acoustic signatures. In the following, we consider that the Young modulus, the Poisson's ratio, and the density of gold are, respectively, 79 GPa, 0.44, and $19\ 300\ \text{kg/m}^3$.²⁷ The longitudinal v_L and transverse v_T sound velocities are then $3.6\ \mu\text{m ns}^{-1}$ and $1.2\ \mu\text{m ns}^{-1}$, respectively. Thus, the higher 16 GHz frequency appears to be the thickness vibration of the beam owing to the fact that $v_L/(2h) = 16.5\ \text{GHz}$. The displacement field of this d_2 eigenmode is plotted in Fig. 3(b). At this point, we verify that this thickness resonance signature is also observed when the pump-probe experiment is undertaken on the gold mesa using an interferometric scheme in this case as photoelastic signals are negligible in gold layers.²⁸ Consequently, the reflectometry measurement undertaken on the gold nanobeam is probably partly an interferometric like detection with the light reflected by the silicon substrate underneath acting as a reference mirror.

The case of the lower frequency $\sim 3\ \text{GHz}$ is dealt with by performing an eigenmode analysis by finite elements method. The dispersion relation of a 370 nm wide nanobeam is plotted in Fig. 3. Several acoustic modes with non-zero cut-off frequencies are revealed. Three distinct families emerge: the flexural modes f_1 , f_2 , and f_3 , the dilatational modes d_1 and d_2 , and the shear modes s_1 , s_2 , and s_3 (see Fig. 3(b)). The frequency evolution of s_1 , s_2 , f_1 , f_2 , f_3 , and d_1 with the nanobeam width is plotted in Fig. 4. The measured frequencies on different gold nanobeams are also reported. Owing to the measurement uncertainties, the experimental frequencies ranging from 1.7 GHz to 5.5 GHz may be

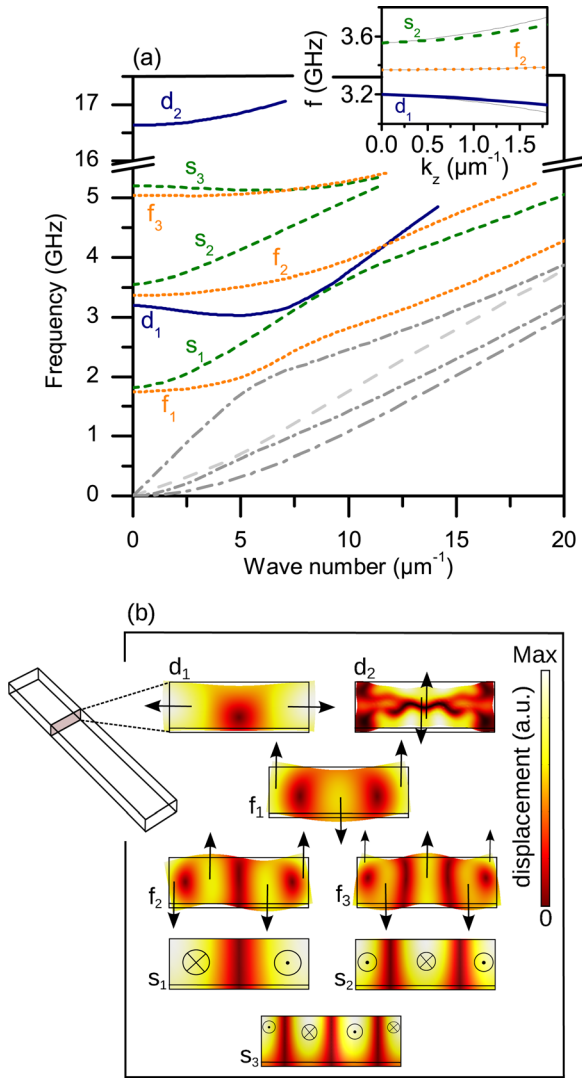


FIG. 3. (a) Acoustic modes dispersion relations in a 370 nm wide and 110 nm thick gold nanobeam (with a 10 nm thick adhesion layer of chromium). f_i , s_i , and d_i refer, respectively, to flexural, shear, and dilatational modes. The inset shows the parabolic fit of three specific modes at low wave number used to evaluate the corresponding propagating wave packet. The parabolic fit is, respectively, $f_{d_1}(k) = -3.4 \times 10^{-2} k^2 - 9.2 \times 10^{-5} k + 3.2$ GHz, $f_{s_2}(k) = 5.0 \times 10^{-2} k^2 + 5.0 \times 10^{-4} k + 3.6$ GHz, and $f_{f_3}(k) = 5.7 \times 10^{-3} k^2 + 2.8 \times 10^{-4} k + 3.4$ GHz for the modes d_1 , s_2 , and f_3 with the wave number k in μm^{-1} . (b) Cross-sectional representation of the displacement field of three flexural (f_1 , f_2 , and f_3), two dilatational (d_1 and d_2), and three shear (s_1 , s_2 , and s_3) acoustic modes. The black arrows show the displacement direction.

consistent with the frequencies of the modes f_2 , s_2 , and d_1 which exhibit close cut-off frequencies. Consequently, additional evidence on the detected mode is needed. Given that the excitation process imposes the relative amplitudes of the excited modes, one can use the initial displacement field projection on the orthogonal basis formed by the nano-object eigenmodes to identify which mode will be efficiently excited.^{29,30} Here, we propose to discriminate unambiguously between the different acoustic modes by probing their propagation. Very different behaviors are expected owing to the very different slopes of the dispersion relationship.

In order to be sensitive to the propagation phenomenon, the pump and probe beams have to be separated.⁸ The transient reflectivity measured on a 370 nm width gold nanobeam, with pump-probe separation ranging from 0 μm to

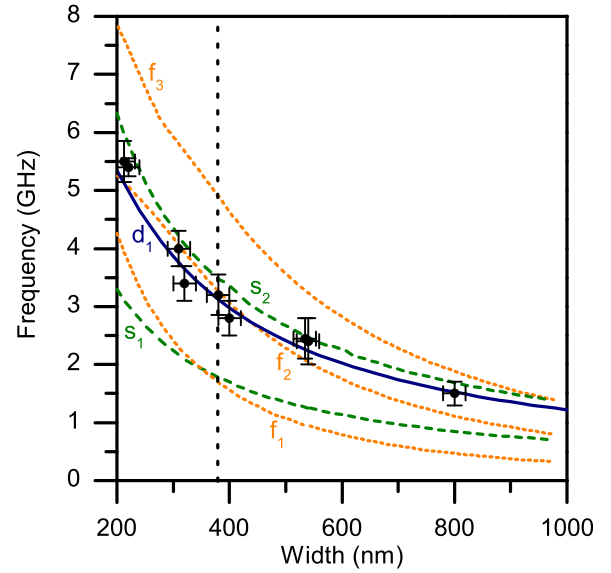


FIG. 4. Using a finite elements method, the acoustic mode frequency at wave number $k=0$ is plotted versus the nanobeam width. Flexural, shear, and dilatational modes are, respectively, the orange dotted lines, the green dashed lines, and the blue solid lines. Experimental measurements are the full black circle with bars. The vertical black dashed line at 370 nm is the specific width where dispersion relations have been calculated (Fig. 3) and propagation has been observed (Fig. 5).

2.1 μm , is presented in Fig. 5(a). The vertical scale corresponds to the pump-probe spatial separation. The exponential thermal background has been removed. As physical insight on the attenuation process is beyond the scope of this study, each transient reflectivity signal is normalized by its maximum: the eighth experimental signal with 2.1 μm spatial separation is 1 order of magnitude less intense than the first one when pump and probe beams are spatially superimposed. The signal is mainly composed by a 3.2 GHz oscillation. As the pump-probe separation increases, this wave-packet shifts to a longer time delays as expected for a propagation guided along the nanobeam. This is analogous to what has already been observed in copper nanowires.¹⁵ However, let us have a closer look at the individual wave fronts (Fig. 5(e)). It appears that as the wave-packet propagates (from darker to lighter curve), the individual wave fronts move to smaller time-delay. To investigate this propagation quantitatively, we use the previously developed expression of the reflectivity for a propagating gaussian wave-packet with the parabolic dispersion relation $\omega(k) = \alpha k^2 + \beta k + \gamma$ ¹⁵

$$\Delta r(t) \propto \text{Re} \left(\frac{\exp(-i\gamma t)}{\sqrt{\sigma^2 + 32i\alpha t}} \exp \left(-\frac{8(z_0 - \beta t)^2}{\sigma^2 + 32i\alpha t} \right) \right), \quad (1)$$

where z_0 is the spatial pump-probe separation and σ is the root of the sum of squares of the pump and probe beam diameters at $1/e^2$. A polynomial fit at small wavenumber for d_1 , f_2 , and s_2 (see inset Fig. 3(a)) is used. We then evaluate the theoretical reflectivity signal for these three modes d_1 (Fig. 5(b)), f_2 (Fig. 5(c)), and s_2 (Fig. 5(d)) at different pump and probe separations. The progressive shift of the wave-packet is very slow for the f_2 mode (Fig. 5(c)), due to the very flat dispersion relation. Both the f_2 and s_2 modes show parallel propagation of the individual wave fronts and the

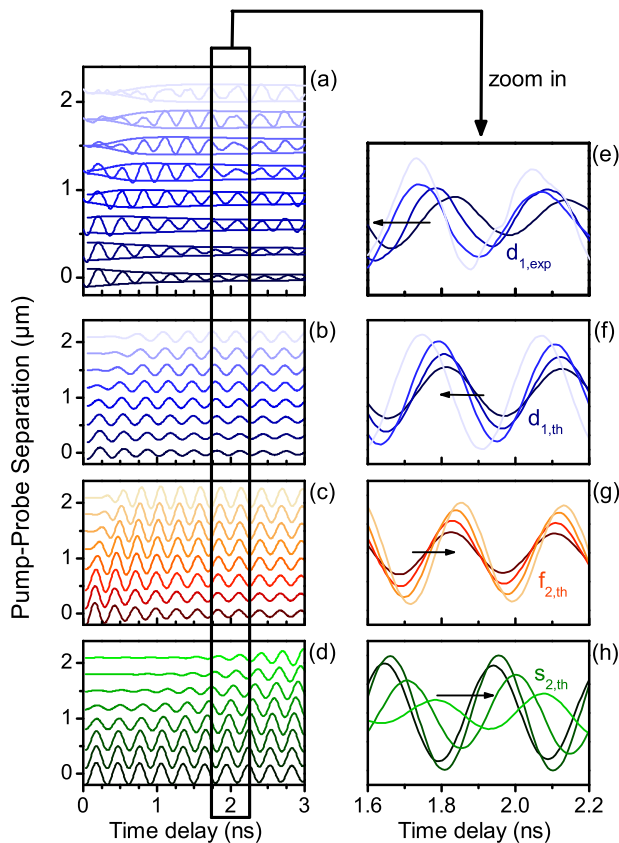


FIG. 5. (a) Experimental transient relative reflectivity signal at different spatial pump-probe separations (the decreasing exponential background has been removed). The offset corresponds to the spatial pump-probe shift and the reflectivity modulation is normalised by the maximum. The envelope of the eight experimental traces in (a) is the simulated envelope of the first dilatational mode d_1 after propagation. (b)–(d) are the simulated transient relative reflectivity signal of the modes d_1 , f_2 , and s_2 , according to the parabolic fit of the dispersion relation (Fig. 3(a)). (e)–(h) are, respectively, the same signals as in (a)–(d) zoomed in a shorter time window. Only half of the eight curves are plotted for readability. The offset is also suppressed in order to observe the propagation direction of the phase of the wave. The black arrow indicates this propagation direction.

wave packet (Figs. 5(g) and 5(h)), whereas the d_1 mode exhibits the expected backward propagation behavior (Fig. 5(f)). According to our simplified analytical expression, the parallel (forward) or anti-parallel (backward) behavior is strongly dependent on the sign of the curvature parameter α . The first dilatational mode d_1 is the only one to exhibit a negative curvature α at low wave numbers k which are the only wave numbers excited owing to the laser spot diameters of around $1 \mu\text{m}$. To confront the experiment, the envelope of the theoretical signal d_1 is also plotted on the experimental oscillation and shows a good agreement (Fig. 5(a)). Finally, it could be argued that the experimental signal is a superposition of two or more acoustic modes. However, if a contribution of beyond 10% of f_2 or s_2 is added in the simulated signal d_1 , the resulting simulated propagative wave no longer exhibits the backward wave behavior. The backward wave observation in our 1D elastic waveguide is thus the unique fingerprint of the first width dilatational mode d_1 .

In conclusion, two dilatational acoustic modes are investigated on e-beam lithographed gold nanobeams by pump-probe time-resolved spectroscopy leading to the observation

of backward wave propagation in the gigahertz range. As a first application, we show unambiguous acoustic mode discrimination using this unique property in the dispersion relations. Furthermore, as already observed in 2D Lamb waveguides, one can imagine to tune the width and thickness of our nanobeam, thus opening the way to negative refraction physics in acoustics at the nanoscale.

The authors would like to thank Michael Rosticher at the ENS for the EBL steps during the maintenance in our facilities, Mélanie Escudier for the gold deposition process, and Frances Edwards for her careful proofreading of the manuscript's English.

- ¹A. Crut, P. Maioli, N. Del Fatti, and F. Vallée, *Phys. Rep.* **549**, 1 (2015).
- ²V. Juvé, A. Crut, P. Maioli, M. Pellarin, M. Broyer, N. Del Fatti, and F. Vallée, *Nano Lett.* **10**, 1853 (2010).
- ³M. van Dijk, M. Lippitz, and M. Orrit, *Phys. Rev. Lett.* **95**, 267406 (2005).
- ⁴P. Siry, L. Belliard, and B. Perrin, *Acta Acust. Acust.* **89**, 925 (2003).
- ⁵A. Vertikov, M. Kuball, A. V. Nurmikko, and H. J. Maris, *Appl. Phys. Lett.* **69**, 2465 (1996).
- ⁶Y. Guillet, C. Rossignol, B. Audoin, G. Calbris, and S. Ravaine, *Appl. Phys. Lett.* **95**, 061909 (2009).
- ⁷T. Bienville, J. F. Robillard, L. Belliard, I. Roch-Jeune, A. Devos, and B. Perrin, *Ultrasonics* **44**(Suppl. 1), e1289 (2006).
- ⁸T. A. Kelf, Y. Tanaka, O. Matsuda, E. M. Larsson, D. S. Sutherland, and O. B. Wright, *Nano Lett.* **11**, 3893 (2011).
- ⁹N. Del Fatti, C. Voisin, F. Chevy, F. Vallée, and C. Flytzanis, *J. Chem. Phys.* **110**, 11484 (1999).
- ¹⁰H. Staleva and G. V. Hartland, *Adv. Funct. Mater.* **18**, 3809 (2008).
- ¹¹P. Zijlstra, A. L. Tchebotareva, J. W. M. Chon, M. Gu, and M. Orrit, *Nano Lett.* **8**, 3493 (2008).
- ¹²T. A. Major, A. Crut, B. Gao, S. S. Lo, N. Del Fatti, F. Vallée, and G. V. Hartland, *Phys. Chem. Chem. Phys.* **15**, 4169 (2013).
- ¹³L. Belliard, T. W. Cornelius, B. Perrin, N. Kacemi, L. Becerra, O. Thomas, M. Eugenia Toimil-Molares, and M. Cassinelli, *J. Appl. Phys.* **114**, 193509 (2013).
- ¹⁴O. Ristow, M. Merklein, M. Grossmann, M. Hettich, M. Schubert, A. Bruchhausen, J. Grebing, A. Erbe, D. Mounier, V. Gusev, E. Scheer, T. Dekorsy, and E. C. S. Barretto, *Appl. Phys. Lett.* **103**, 233114 (2013).
- ¹⁵C. Jean, L. Belliard, T. W. Cornelius, O. Thomas, M. E. Toimil-Molares, M. Cassinelli, L. Becerra, and B. Perrin, *J. Phys. Chem. Lett.* **5**, 4100 (2014).
- ¹⁶P.-A. Mante, Y.-C. Wu, Y.-T. Lin, C.-Y. Ho, L.-W. Tu, and C.-K. Sun, *Nano Lett.* **13**, 1139 (2013).
- ¹⁷A. Amziane, L. Belliard, F. Decremps, and B. Perrin, *Phys. Rev. B* **83**, 14102 (2011).
- ¹⁸V. Veselago and E. Narimanov, *Nat. Mater.* **5**, 759 (2006).
- ¹⁹V. G. Veselago, *Sov. Phys. Usp.* **10**, 509 (1968).
- ²⁰C. G. Parazzoli, R. B. Gregor, J. A. Nielsen, M. A. Thompson, K. Li, A. M. Vetter, M. H. Tanielian, and D. C. Vier, *Appl. Phys. Lett.* **84**, 3232 (2004).
- ²¹H. Lamb, *Proc. London Math. Soc.* **2**, 473 (1904).
- ²²A. H. Meitzler, *J. Acoust. Soc. Am.* **38**, 835 (1965).
- ²³A. A. Maznev and A. G. Every, *Appl. Phys. Lett.* **95**, 011903 (2009).
- ²⁴F. D. Philippe, T. W. Murray, and C. Prada, *Sci. Rep.* **5**, 11112 (2015).
- ²⁵S. Bramhavar, C. Prada, A. A. Maznev, A. G. Every, T. B. Norris, and T. W. Murray, *Phys. Rev. B* **83**, 014106 (2011).
- ²⁶C. Thomsen, J. Strait, Z. Vardeny, H. J. Maris, J. Tauc, and J. Hauser, *Phys. Rev. Lett.* **53**, 989 (1984).
- ²⁷M. A. Meyers and K. K. Chawla, *Mechanical Behavior of Materials* (Cambridge University Press, Cambridge, 2009), Vol. 2.
- ²⁸B. Perrin, C. Rossignol, B. Bonello, and J. C. Jeannet, *Physica B* **263–264**, 571 (1999).
- ²⁹M. Hu, X. Wang, G. V. Hartland, P. Mulvaney, J. P. Juste, and J. E. Sader, *J. Am. Chem. Soc.* **125**, 14925 (2003).
- ³⁰A. Crut, V. Juvé, D. Mongin, P. Maioli, N. Del Fatti, and F. Vallée, *Phys. Rev. B* **83**, 205430 (2011).